communications earth & environment

Article

A Nature Portfolio journal

https://doi.org/10.1038/s43247-025-03119-x

Evidence for landslides triggered by impact events on Ceres

Marco Emanuele Discenza [1], Maria Teresa Brunetti [2] ✉, Lisa Molaro [3], Mariacarmela Minnillo[1], Goro Komatsu [4] & Enrico Miccadei[5]

Triggering mechanisms are a fundamental aspect of landslide studies, as they directly influence both the characteristics of landslides and the environments in which they occur. Identifying the triggers of landslides is particularly important for understanding the morphological evolution of solid planetary surfaces in the Solar System. Ceres, the largest celestial object in the main asteroid belt, is rich in impact craters and exhibits numerous landslides. Published catalogues and available data on these surface features provide a unique opportunity to study the interactions between meteoroid impacts and mass movements. By analyzing the morphometric characteristics and absolute dating of eight landslides and their related impact craters, we have identified an evident cause-and-effect relationship between impact events and the initiation of landslides on Ceres.

Landslides, i.e., mass movements of rock, debris, or soil along a slope under the action of gravity[1], are geomorphic features not unique to Earth. Landslide occurrence has been documented on many solid bodies across the Solar System, including terrestrial planets, dwarf planets, moons, asteroids, and comets[2]. On Earth, landslides are generally classified according to the type of mass movement, including falls, topples, slides, spreads, flows, and slope deformations or a combination of these[3]. Planetary and other extraterrestrial solid surfaces are also affected by similar types of mass movements[4–12]. Nevertheless, an important yet understudied aspect of extraterrestrial landslides pertains to their triggering mechanisms, which directly influence both the characteristics of the failures and the environments in which they occur[13]. Understanding the triggers and development of landslides is important for interpreting the morphological evolution of solid surfaces in the Solar System.

Mass movements on planetary surfaces are triggered by a variety of factors that depend on the planetary complexity and its specific characteristics[14]. Surface processes, including tectonics, volcanism, meteoroid impacts, erosion, cryovolcanism, slope debuttressing, and gravity, act to a greater or lesser extent on the destabilization of the slopes[2,7,15]. The effects of meteoroid impacts have been demonstrated to be particularly relevant on bodies with minimal or no atmosphere, potentially leading to fracturing of existing slopes, producing ground shaking[4] and also generation of new slopes inside the forming craters. On planets such as Mars and Venus, endogenic seismic and volcanic activity may have caused ground motions, which led to the observed giant landslides[16,17]. The solar-induced thermal stress can cause the expansion and contraction of rocky surface materials and, over time, can lead to the weakening of slopes[18]. On Mars, the expansion and collapse of subsurface cryosalt has been hypothesized as a possible trigger for landslides[19].

On the dwarf planet Ceres, impacting of meteoroids gives rise to the formation of steep slopes, and the release of kinetic energy has the potential to destabilize surface materials, which in turn leads to landsliding. The accumulation of debris from past impact events, as well as the progressive weakening of regolith due to thermal cycling, may create conditions favorable for slope failure[6]. This, in combination with localized seismic shaking, can further contribute to the triggering of landslides[20]. High-impact energies can also induce transient melting of ice within the crust, thereby reducing material cohesion and facilitating downslope movement[21].

High-resolution images of the Ceres surface taken by NASA's 2007 Dawn spacecraft framing camera[22] provided visual evidence of impact craters and geomorphological processes[23–25], including landslides[20,26] on the surface. Along with the impact craters, which dominate the topography of Ceres, and talus deposits due to crater wall retreats[27], landslides represent the most prevalent geologic features, occurring in more than 20% of craters larger than 10 km in diameter[20]. Several landslide inventories available for Ceres[6,20,26] highlight that mass movements are distributed over the entire surface of the dwarf planet (Fig. 1). Many authors have identified and classified three types of flow-like mass movements on Ceres on the basis of their morphology: Type 1 (T1) and Type 2 (T2), both of which are consistent with slope failure, and Type 3 flows (T3), which have been interpreted as being associated with ejection and fluidization rather than slope failure[28].

In one recent inventory built on earlier works, 210 mass wasting features were mapped and classified into three distinct classes[29]: slumps, slides, and flow-like movements. Slumps and slides are particularly pronounced at mid-latitudes and barely detectable at the poles, supporting a speculation about vertical ice variations on Ceres surface[25]. The flow-like movements are

[1]Geoservizi S.r.l., Ripalimosani, Italy. [2]National Research Council, Research Institute for Geohydrological Protection, Perugia, Italy. [3]University of Trento, Trento, Italy. [4]Università degli Studi G. D'Annunzio Chieti-Pescara, Pescara, Italy. [5]Università degli Studi G. D'Annunzio Chieti-Pescara, Chieti Scalo, Italy. ✉e-mail: mariateresa.brunetti@cnr.it

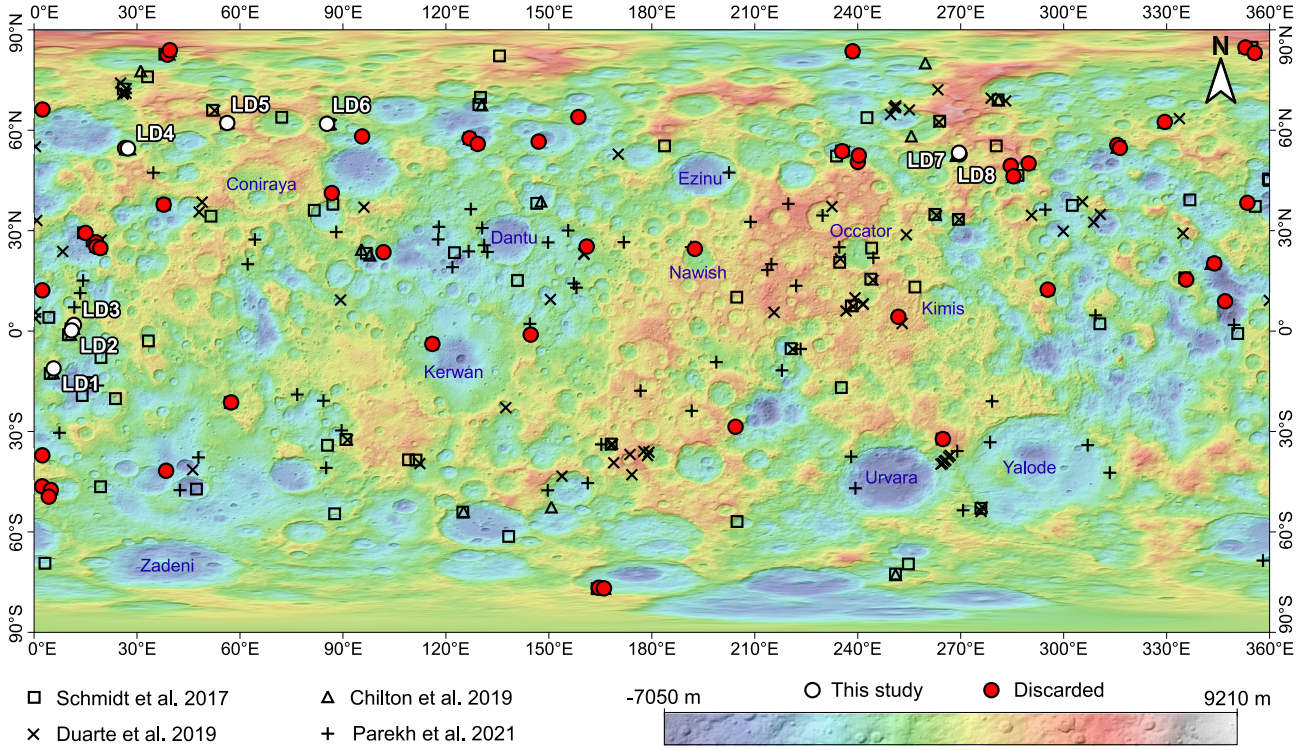

Fig. 1 | Distribution of landslides on Ceres. The map highlights landslides analyzed and dated in this study, as well as those that show spatial correlation with impact craters, but were discarded (see "Methods"). The image was produced with the HAMO (High Altitude Mapping Orbit) global digital terrain model, superposed on the HAMO colorized shaded-relief image. The map also includes the major landslide inventories[6,20,26,29]. Source: NASA/JPL-Caltech/UCLA/MPS/DLR/IDA.

characterized by the presence of multiple surface striations in the direction of movement, which is the main morphological trait different from slides and slumps. There is geomorphic evidence that Ceres interior is ice-rich and that cryovolcanism has been active on the surface of this body[30]. Among the dynamics of landslide processes on Ceres, the influence of ice-rich crustal materials has yet to be studied.

Landslides on Ceres are typically located either inward or outward at the rim and/or ejecta of impact craters[29]. The trigger for these failures is most likely the impact of a meteoroid, which may result in fracturing a slope, often the wall of a nearby older crater, leading to the occurrence of the slope failure. Based on pieces of morphological evidence, the initiation of a landslide in response to an impact event can be of two main types. The first type is a direct strike producing local rock fragmentation and ground deformation, followed by landsliding. This type is poorly studied in the literature[20,31,32] and is rarely described as a cause of landslides, despite geological and morphological evidence indicating its widespread occurrence on solid bodies across the Solar System. In the second type, failure occurs in the surrounding terrain, which may result from impact-induced seismic activity[2,4,12,15,33]. Previous works that have dated landslides on Mars[33–36] have hypothesized the second type of process, in which the trigger is due to ground shaking on potentially unstable slopes induced by meteoroid impact in the surrounding terrain. Some authors[37] studied the long-runout landslide of the Tsiolkovsky crater on the Moon, which is an example of the first type of process. While they do not present specific considerations on the trigger, they hypothesize that the landslide occurred soon after the crater was formed.

By analyzing the first type of trigger, our findings are consistent with a cause-and-effect relationship between the impact event process and the occurrence of landslides. The establishment of this relationship is possible through a morphological analysis, which links the occurrence of landslides to adjacent impact events, and by dating their surface features, which allows a sequence of events to be determined.

The crater size-frequency distribution (CSFD) within an area of interest is the method currently used to determine the absolute model age of the area[38]. On Ceres, we analyze the morphology and the age of eight among 57 landslides classified as the first type of trigger. The selected case studies are based on the criteria that would enable us to determine their absolute model age with sufficient detail to support the proposed hypotheses of temporal correlation between the two processes (see Methods). Some of the features analyzed in this study were previously dated[39], even though they did not make any specific assessment on the trigger. The novelty here lies in using CSFD to date both landslides and the impact craters that presumably caused them. This leads us to establish a cause-and-effect relationship between the two phenomena.

This study represents an important contribution to the field, attempting to date landslides on Ceres and relate them to coeval impact events. Morphological analysis and age determination of selected case studies establish that triggering of the landslides was by nearby meteoroid impacts.

Results

To reveal the cause-and-effect relationship between meteoroid impacts and nearby landslide initiation, we select case studies where landslides are located in close proximity to impact craters. Among the 57 documented landslides with nearby craters (Fig. 1), we analyze eight cases where absolute dating through crater counting could be reliably performed (see "Methods"). Landslides are located in the equatorial region of Ceres and at mid-latitudes in the northern hemisphere. The morphological analysis allows the eight landslides to be associated with six impact events that have presumably triggered the slope failures (Fig. 2). The failures initiated along the outer part of the rim of the presumably triggering craters, and in most cases they developed on the internal wall of a pre-existing crater.

The dating of the crater ejecta and the landslide deposits allows us to perform a chronological comparison of the two processes. The absolute model ages of the studied landslides using the CSFD method range from $13.8^{+6.0}_{-4.6}$ Ma to 108^{+18}_{-16} Ma, considering all impact craters, and from $13.5^{+7.2}_{-5.3}$ Ma to 107^{+36}_{-29} Ma, considering only primary craters (Table 1). In general, except for a few cases where there are many SICs and FSICs, the two sets of age data are fairly congruent. In both approaches, the

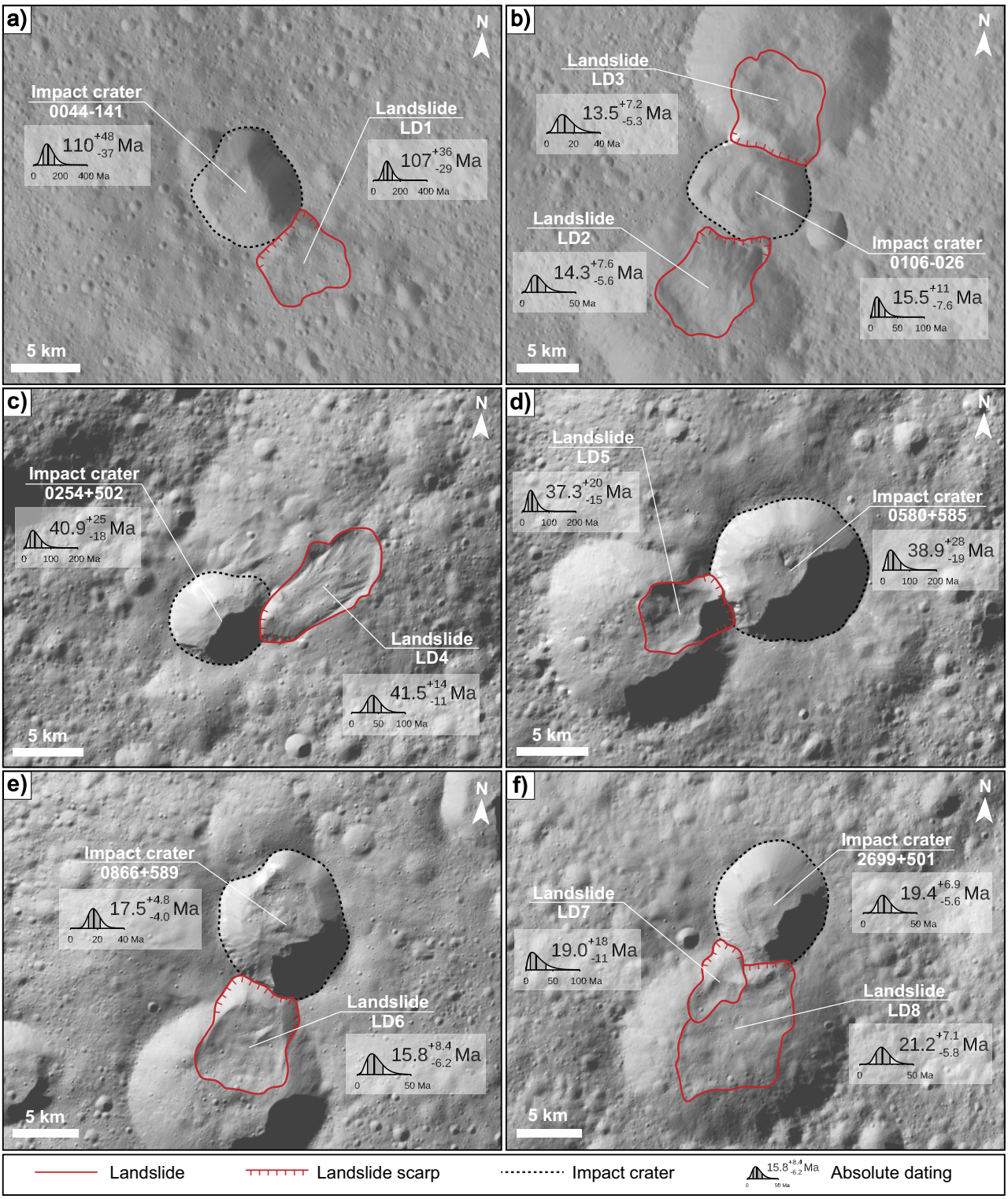

Fig. 2 | Landslides presumably triggered by nearby impact craters and their absolute model ages. The maps show impact craters (black dotted lines) related to the trigger of landslides (red solid lines). Panels refer to: **a** LD1; **b** LD2 and LD3; **c** LD4; **d** LD5; **e** LD6; **f** LD7 and LD8. The image was produced with the LAMO (Low Altitude Mapping Orbits) global mosaic. Source: NASA/JPL-Caltech/UCLA/MPS/DLR/IDA.

estimated absolute model ages are relatively low and show rather young landslides (<~150 Ma).

Six craters are identified as resulting from impacts that were responsible for triggering eight landslides (Table 1). Of these craters, four are associated with single landslides, while two are related to pairs of landslides. The estimated absolute model ages of the crater ejecta using all impact craters (primary and SICs/FSICs), range from $19.7^{+5.8}_{-4.8}$ Ma to 84.7^{+11}_{-10} Ma. When considering only primary impact craters, the ejecta ranges from $15.5^{+11}_{-7.6}$ Ma to 110^{+48}_{-37} Ma. Notably, the age range of ejecta is consistent with that for the landslides within the error margins, thereby confirming a temporal proximity of the two events.

Table 1 | Summary of absolute model ages of landslides and craters of triggering impacts

ID	S_A km²	A_A Ma	S_P km²	A_P Ma
LD1	24.36	108^{+18}_{-16}	6.93	107^{+36}_{-29}
0044−141	62.35	84.7^{+11}_{-10}	17.96	110^{+48}_{-37}
LD2	39.24	$18.1^{+6.8}_{-5.4}$	28.69	$13.5^{+7.2}_{-5.3}$
LD3	38.17	$13.8^{+6.0}_{-4.6}$	25.83	$14.3^{+7.6}_{-5.6}$
0106−026	23.88	$26.2^{+7.7}_{-6.4}$	11.72	$15.5^{+11}_{-7.6}$
LD4	35.71	$40.8^{+9.6}_{-8.3}$	18.13	41.5^{+14}_{-11}
0254+502	24.47	39.7^{+12}_{-10}	10.46	40.9^{+25}_{-18}
LD5	17.44	35.6^{+13}_{-11}	8.97	37.3^{+20}_{-15}
0580+585	148.17	34.4^{+25}_{-17}	92.90	38.9^{+28}_{-19}
LD6	40.77	$22.6^{+6.9}_{-5.7}$	25.37	$15.8^{+8.4}_{-6.2}$
0866+589	78.21	$21.9^{+5.0}_{-4.1}$	55.08	$17.5^{+4.8}_{-4.0}$
LD7	12.96	25.8^{+14}_{-10}	2.64	19.0^{+18}_{-11}
LD8	59.54	$26.1^{+6.0}_{-5.2}$	36.08	$21.2^{+7.1}_{-5.8}$
2699+501	52.39	$19.7^{+5.8}_{-4.8}$	37.47	$19.4^{+6.9}_{-5.6}$

ID is LDn for landslides and a numeric code for craters[44]. S_A is the area used for crater counting when considering all the impact craters (i.e., including SICs/FSICs); A_A is the absolute age of the landslide and of the crater determined in S_A; S_P is the area used for crater counting when considering only primary impact craters; A_P is the absolute age of the landslides and of the crater determined in S_P. Alternating rows list landslides and their corresponding triggering craters.

In order to establish a cause-and-effect correlation between the selected eight landslides and associated impact craters, their absolute model ages are calculated through CSFD (Fig. 3) and then compared in terms of absolute values and statistical uncertainty (Table 1). Our investigation utilizes only primary craters to improve temporal accuracy[40–43]. A detailed description of each case analyzed is given below.

Landslide LD1

LD1 (Fig. 2a) is a complex feature situated along the outer, south-eastern margin of a well-defined impact crater approximately 8.2 km in diameter (ID:0044-141[44]). Along the north-western flank, the impact structure cuts a further, smaller crater roughly 4.0 km wide. The interior of the crater is marked by a flow landslide in its northern sector and by infill deposits. Neither the landslide in the main crater nor that in the northwest crater is analyzed or dated, as both are shallow and have poorly-defined boundaries. Outside and around the 0044-141 crater, an extensive ejecta blanket is present, with greater thickness in the northern section. For this crater, the thicker and more conspicuous northern ejecta, as well as the crater floor have been dated.

LD1 is dated to be 107^{+36}_{-29} Ma, which is consistent with the absolute model age 110^{+48}_{-37} Ma of the 0044-141 crater (Fig. 3a).

Landslides LD2/LD3

LD2 and LD3 (Fig. 2b) are the most intriguing case among those analyzed in terms of correlation with an impact crater. These are, in fact, two complex features located on the NNE and SSW external edges of a single impact crater slightly elongated in the WNW-ESE direction with a maximum diameter of approximately 8.0 km (ID:0106-026[44]). The two landslides fall within two larger and older impact structures, with diameters of 14.4 km (ID:0100-038[44]) and 15.5 km (ID:0108-014[44]). The interior of the triggering crater located between the two landslides is filled with apparently recent deposits, while the exterior is characterized by a thick ejecta more evident in the eastern part. The two largest craters in which the landslides occur have not been dated, as they are not relevant for the purpose of the study. For the central crater, only a part of the ejecta located to the east has been analyzed, as it is thicker and favors better absolute dating.

LD2 has an absolute model age of $13.5^{+7.2}_{-5.3}$ Ma, and LD3 has an absolute model age of $14.3^{+7.6}_{-5.6}$ Ma. In both cases, the dating is consistent with the absolute model age $15.5^{+11}_{-7.6}$ Ma of the 0106-026 crater (Fig. 3b).

Landslide LD4

LD4 (Fig. 2c) is a flow-type feature located along the outer, eastern rim of a well-defined impact crater with a diameter of approximately 6.8 km (ID:0254 + 502[44]). This landslide extends in a SW-NE direction and develops inside an older and larger impact crater with a maximum diameter of approximately 29.2 km (ID:0277 + 514[44]). To the NW of the studied landslide, there are two other, less evident, flow-type landslides that are not analyzed in this study. The inner part of the 0254 + 502 crater is filled with deposits, while on the outside, there are ejecta, which are generally not very thick and are particularly evident near the rim. For the 0254 + 502 crater, the most visible portion of the ejecta located near the rim in the NW region is dated.

LD4 is dated to be 41.5^{+14}_{-11} Ma, which is very consistent with the absolute model age 40.9^{+25}_{-18} Ma of the 0254 + 502 crater (Fig. 3c).

Landslide LD5

LD5 (Fig. 2d) is a slide-type feature located along the outer, south-western margin of a well-defined impact crater with a maximum diameter of approximately 10.3 km (ID:0580 + 585[44]). The impact structure analyzed is contiguous to another crater, slightly larger and with an NW-SE elongated shape, with a maximum diameter of approximately 12.0 km (ID: 0555 + 579[44]). LD5 develops in an approximately NE-SW direction within this second crater, which does not show any further slope movement of appreciable size. Outside the 0580 + 585 crater, there is a well-defined ejecta with considerable thickness, especially in the sector closest to the rim. The ejecta of the 0580 + 585 crater is dated by analyzing the most proximal portion, excluding only the area occupied by LD5.

LD5 is dated to be 37.3^{+20}_{-15} Ma, which is consistent with the absolute model age 38.9^{+28}_{-19} Ma of the 0580 + 585 crater (Fig. 3d).

Landslide LD6

LD6 (Fig. 2e) is a sliding feature located along the outer, SSW margin of a well-defined impact crater approximately 11.0 km in diameter (ID:0866 + 589[44]). The crater has an irregular shape, probably related to mass wasting processes on the inner walls of the rim, which favored accumulation of thick deposits inside the crater. The landslide develops in a direction approximately NNE-SSW inside a second contiguous older crater, with a diameter of approximately 15.1 km (ID:0857 + 572[44]). Outside the 0866 + 589 crater, ejecta blanket is clearly visible, especially near the rim in the western and most proximal portion of the ejecta. The ejecta of the

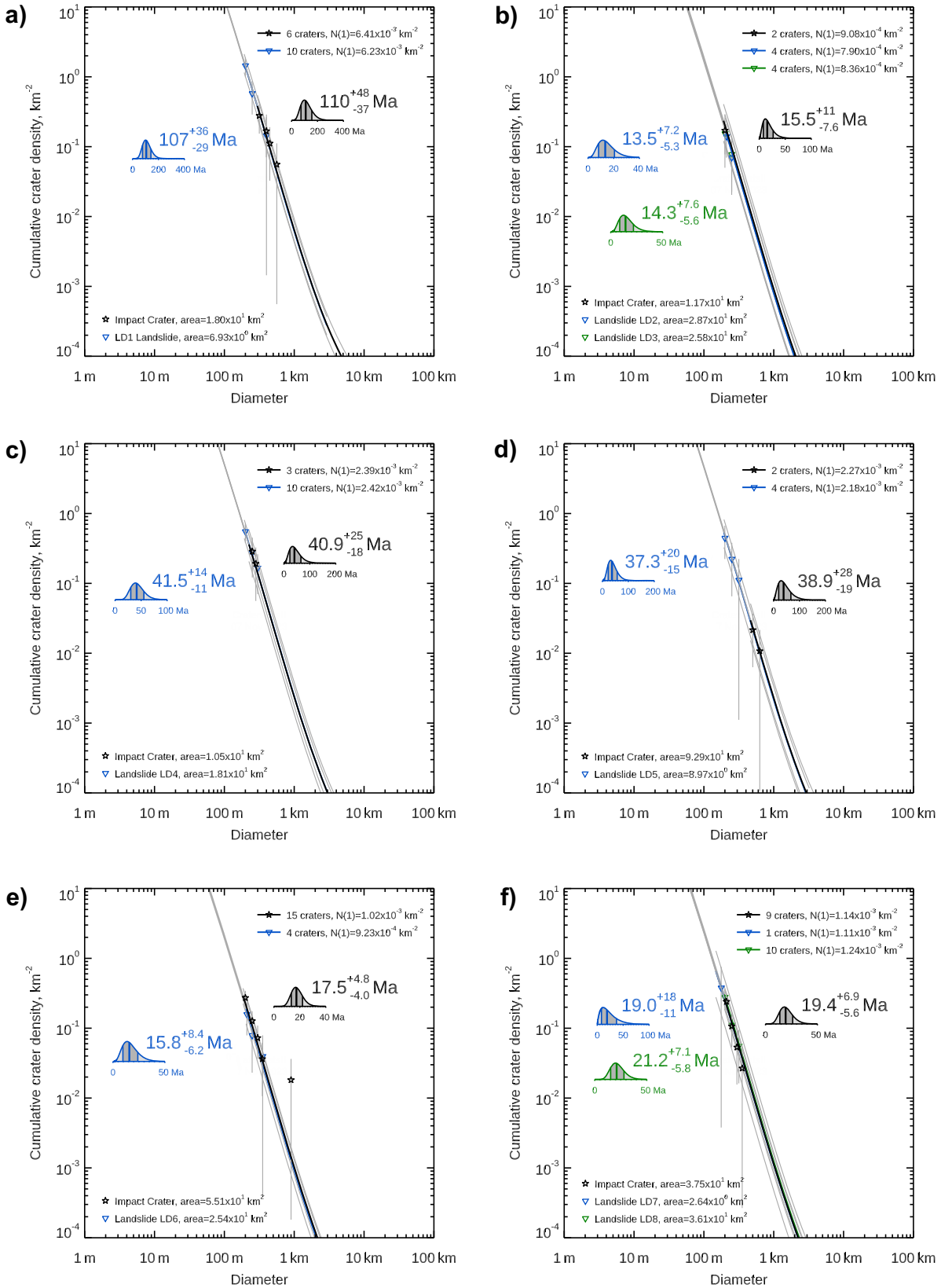

Fig. 3 | Comparison of absolute model ages of landslides and related impact crater ejecta. Graphs refer to: **a** LD1; **b** LD2 and LD3; **c** LD4; **d** LD5; **e** LD6; **f** LD7 and LD8. Blue and green colors are used for landslides, and black for impact crater ejecta.

0866 + 589 crater is dated by analyzing the western and most proximal portion.

LD6 has an age of $15.8^{+8.4}_{-6.2}$ Ma, which is consistent with the 0866 + 589 crater absolute model age of $17.5^{+4.8}_{-4.0}$ Ma (Fig. 3e).

Landslides LD7/LD8

LD7 and LD8 (Fig. 2f) are very peculiar features, as they constitute a pair of landslides closely connected to an impact crater. LD7 and LD8 are two complex phenomena situated on the outer, SSW edge, of a well-defined

Table 2 | Summary of landslide morphometry

ID	Coordinates (lat, lon)	Landslide type	H (km)	L (km)	H/L (-)	W_s (km)	W_t (km)	S_l (km^2)
LD1	−14.865, 4.899	Complex	0.93	5.93	0.16	5.32	6.36	27.92
LD2	−3.477, 10.297	Complex	1.37	8.28	0.17	5.49	6.78	48.05
LD3	−1.747, 10.846	Complex	0.90	8.18	0.11	7.08	7.56	49.18
LD4	50.605, 26.962	Flow	3.26	10.96	0.30	3.09	5.38	40.60
LD5	58.134, 56.327	Slide	1.25	6.43	0.19	4.17	5.06	27.51
LD6	57.829, 85.993	Slide	1.67	8.45	0.20	6.48	7.17	52.43
LD7	49.486, 269.281	Complex	1.93	6.92	0.28	3.17	4.04	17.06
LD8	49.008, 269.609	Complex	0.75	9.91	0.08	6.46	7.68	74.26

H height along the central axis, *L* length along the central axis, *H/L* ratio between the drop height and the length, W_s width along the scar, W_t width along the deposit, S_l overall area.

impact crater with a diameter of about 9.6 km (ID:2699 + 501[44]). The two landslides are partially overlapping and developing in a direction approximately NNE-SSW, inside a second, older crater, contiguous to the previous one and with a diameter of about 14.2 km (ID: 2693 + 488[44]). The interior of the 2699 + 501 crater is characterized by thick fill deposits, probably connected to mass-wasting processes that affected the interior of the rim. Outside, there is an irregular ejecta deposit, which is only clearly visible in the area closest to the impact structure. Regarding the 2699 + 501 crater, the most visible part of the ejecta, close to the crater rim, is dated.

LD7 has an absolute model age of 19.0^{+18}_{-11} Ma, while LD8 has an absolute model age of $21.2^{+7.1}_{-5.8}$ Ma. In both cases, the dating is consistent with the absolute model age of the 2699 + 501 crater, which is $19.4^{+6.9}_{-5.6}$ Ma (Fig. 3f).

Discussion

The selection of landslides in this study is based on morphological analysis that establishes a spatial correlation between the mass movement and a nearby impact event of the first type. Surface dating allows the assessment of causal relationships between the occurrence of slope failures and coeval meteoroid impacts. The analyzed landslides exhibit clear morphological and morphometric characteristics (see "Methods"), which allow a cross-analysis relative to the closest impact craters for the study of potential triggering mechanisms. The mapping of the landslides and the resulting morphometric parameters are in good agreement with previous findings on Ceres landslides[6,20,26,29]. The data in Table 2 currently reveal no correlations between landslide type, area, mobility, or latitude. However, it cannot be ruled out that future analyses could benefit also from this information.

The detailed mapping of the landslides and their deposits enables highly accurate crater counting on all areas of interest. The analyzed dataset highlights that the spatial relationship between impact craters and landslides is present for several landforms on the surface of Ceres. However, the selection of landslides is constrained by the feasibility of performing a proper crater counting, thus correctly dating the features.

The morphology of landslides and related impact craters implies a strong correlation between the two processes. Their proximity, relative position, and size of these two types of landforms, in fact, support the hypothesis of a trigger due to meteoric impact. In all cases, the landslides develop on the external edge of the rim connected to the crater that is supposed to have triggered the landslide. In most cases, the mass movements develop inside a second, pre-existing and older impact crater[20]. Only in one case (LD1) among those studied the landslide develop on a surface with a low inclination, without the presence of an older impact crater. This implies that the presence of pre-existing steep inner slopes of older craters is facilitating landslide occurrence.

The landslides that have been studied are very recent, having occurred within the last 150 million years, and they show few signs of subsequent modification due to weathering processes. Secondary scarps have not been observed, except for a small one on the north-eastern side of LD2, which does not affect the overall morphology of the failure. The only case showing evidence of subsequent reactivation is LD7, which overlaps LD8. In this case, we mapped the landslides separately to minimize potential dating errors. The absence of secondary disturbances that could affect crater counts and complicate age estimates reinforces our confidence in the dating results.

The same dating method is used for both the landslides and craters, which, according to the morphological analysis, are most likely responsible for slope failures. The estimated absolute model ages of all the landforms (landslides and craters) using two dating approaches (i.e., using primary crater data only or also using SICs/FSICs) are relatively low, and they indicate rather young landslides (<~150 Ma). In all eight cases studied, the dating results of the landslides and their relative triggering impact craters show that they are coeval within the margins of error (Fig. 4).

Notably, the dataset includes two cases (LD2/LD3 and LD7/LD8) where a meteoroid impact caused two landslides. Specifically, for the LD2/LD3 system, the coeval age of the landslides and the crater (0106-026) is consistent with the geomorphological, dimensional, and kinematic evidence (see Table 2 in the "Methods"), suggesting that the two landslides are associated with the same triggering impact. For the LD7/LD8 system, the larger feature (LD8) is directly connected to the impact crater (2699 + 501), as it has no ejecta covering and therefore cannot be older than the impact. The smaller feature (LD7), however, could be coeval with the previous one (developed immediately after LD8) or subsequent to it. Currently, no information is available to absolutely define the genesis of LD7.

In the case studies, the observed directional asymmetry of the landslides is due to the morphological condition in which the triggering impact occurs, i.e., the orientation of the pre-existing slope. The majority of landslides develop along the slope within the pre-existing crater where greater relief energy and topographical conditions are favorable for gravity-driven mass movements. This is evident in only the case of two landslides with opposite orientations (LD2 and LD3), where the triggering impact is centered in between the two pre-existing craters. In the context of the present analysis, LD1 represents a unique case, distinguished by the observation that the landslide resulting from the impact does not involve the rim of a pre-existing crater. In this case, the landslide deposit develops in the immediate surroundings of the trigger crater on a surface gently dipping toward SE. Therefore, the landslide developed mainly by exploiting the relief produced by the crater and its rim. In the cases studied, the angle of impact does not appear to influence the direction in which the landslide propagates.

Both LD4 and the ejecta of the nearby crater (ID:0254 + 502) were dated as part of the studies conducted for the production of a geological map of Ceres[39]. Using the lunar-derived model adopted in this study, they found an absolute model age of 37^{+5}_{-5} Ma for the landslide and 53^{+6}_{-6} Ma for the ejecta. The resulting dates from this study differ slightly from those reported in the present study, although they remain consistent within the error margins. It should be emphasized, however, that in the cited study, the entire crater population was used and no specific assessments were conducted for SICs/FSICs, which may explain the slight discrepancy between the dating results.

The 0580 + 585 crater in the proximity of LD5 was previously dated in a study conducted for the preparation of the geological map of Ceres[39].

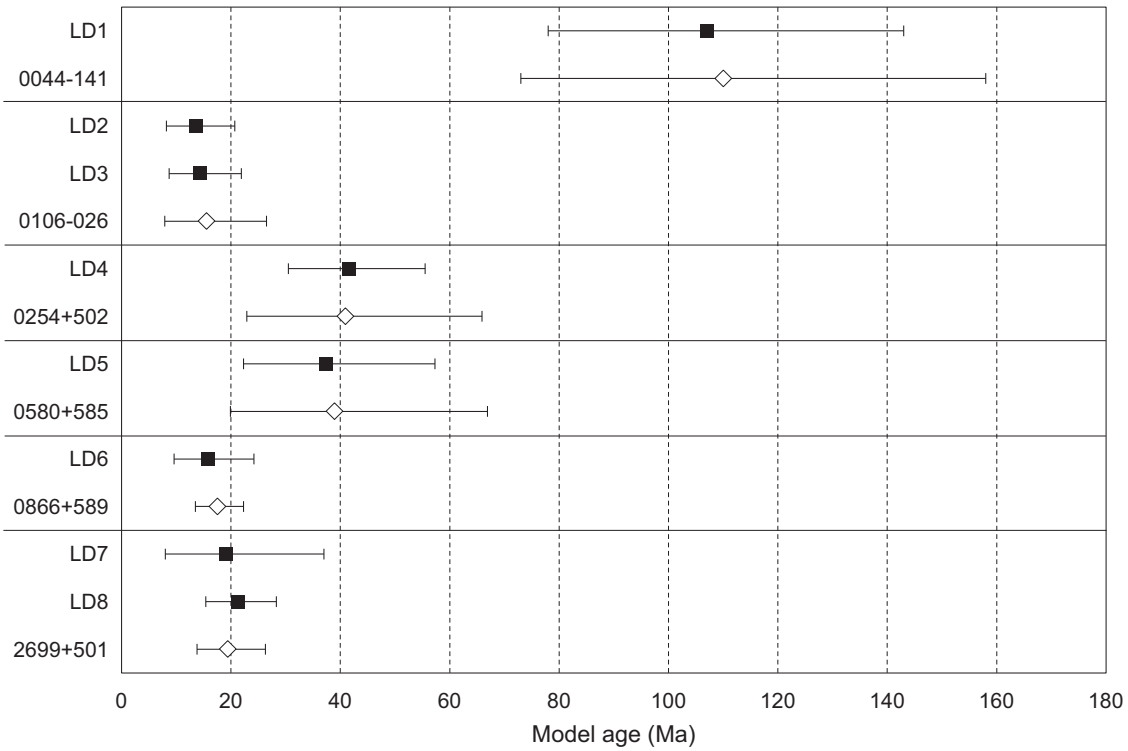

Fig. 4 | Comparison between the absolute model ages of landslides and related impact craters. Black boxes in the graph are used for landslides, and white diamonds for the related impact craters. Error bars represent the uncertainty in the model ages of the features.

Using the lunar-derived model, this impact structure was dated to 13.3^{+3}_{-3} Ma old, which is slightly more recent than 38.9^{+28}_{-19} Ma derived in the present study. The observed discrepancy between the two ages can be attributed to the different techniques employed in the study of the SICs/FSICs (which are instead very similar) and to the subsequent data fitting.

The 0866 + 589 impact crater near LD6 was also dated in the same study[39]. It gave an age of 53^{+4}_{-4} Ma, which is slightly older than $17.5^{+4.8}_{-4.0}$ Ma derived in the present study. The ejecta is characterized by numerous older craters formed in the underlying bedrock unit. This condition can lead to difficulties in the analysis for discriminating the best curve to analyze.

In the present study, the relationship between impact craters and the occurrence of landslides on Ceres is analyzed in detail for selected cases based on the orientation and morphological characteristics (spatial proximity between features and crater rim deformation due to landslide). The study of the landslide inventories available on Ceres[6,20,26,29], highlights the presence of numerous slope failures closely related to impact craters, similarly to the cases described in the present study. However, the number of proposed cases is constrained by the existence of the conditions that allow surface dating and some features have been discarded (Fig. 1). Although the dataset is limited, it can nonetheless be considered a representative sample of the population of landslides presumably triggered by the first type of impact, because it has the same characteristics as the larger group of landslides with adjacent craters, which could not be dated (see Supplementary Figs. 41–45). Thus, dating is performed on a sample chosen independently of the cause-and-effect hypothesis to be demonstrated. In all eight cases, the craters and adjacent landslides are coeval within the limits of methodological uncertainty. Using a binomial distribution, the probability of this occurring by chance for the eight pairs is approximately $3.9 \cdot 10^{-3}$, i.e., extremely low. We maintain that the proposed number of cases sufficiently indicates that there is a cause-and-effect relationship between the impact of a meteoroid and the occurrence of landslides in its vicinity.

Conclusions

Among the most widely accepted triggers of landslides on solid bodies are meteoroid impacts[2,4,12,15,33], in particular, on small bodies such as dwarf planets, asteroids, and comets, due to the absence of other potential causes such as tectonics, volcanism, cryovolcanism, and slope debuttressing. It should be noted that not all impact craters result in landslides unless the necessary conditions are present to ensure the impact is effective (e.g., energy, angle and direction of impact, the predisposition of the surface to landsliding, in terms of slope, previous degree of fracturing).

A systematic study reconstructing the sequence of events through dating landslides and craters to demonstrate a cause-and-effect relationship has been lacking. This study was therefore conducted to identify spatial and temporal evidence supporting the occurrence of landslides triggered by the first type of process.

The absolute dating method has highlighted a close temporal correlation between the formation of the impact craters and the occurrence of the landslides on the outer rim. Overall, the geographical proximity and the morphological setting of the triggering craters and the landslides (morphological criterion), the absolute model ages of both landforms (dating criterion), and the statistical significance of the cases studied (statistical criterion) reasonably allow the exclusion of additional external or endogenic triggers of landslides on Ceres. The data presented, therefore, provide evidence for the presence of landslides on Ceres that were directly triggered by nearby meteoroid impacts. The morphological analysis and subsequent dating of landforms utilized in this study can also be successfully applied to other solid bodies in the Solar System to verify existence of similar cases.

Methods

The methodology used involves the study of landslides that exhibit morphological evidence of the proposed relationship, followed by the absolute dating of their deposits and that of the impact craters that presumably triggered the mass movements. Since a cause-and-effect relationship implies that the features are coeval, the temporal attribute is fundamental to testing the proposed hypothesis. For this reason, a comparative analysis of the absolute model ages of landslides and impact craters is then performed.

Landslide data

Landslides directly associated with nearby impact craters are widespread across the surface of Ceres (Fig. 1). To ensure accurate absolute dating, the main criteria for landslide selection are based on whether crater counting can be properly conducted. No restrictions on typology, size, morphological characteristics, or geographic location are applied. Criteria include: (i) the freshness of the landform, in order to avoid problems related to degradation, erosion, or a number of craters too large (near the saturation limit); (ii) good surface visibility without image distortion; (iii) optimal lighting with few shaded or overexposed areas; and (iv) well-defined outer margins of the feature. All the selected landforms are already present in published inventories[6,20,26,29].

For this study, eight landslides are selected from among numerous cases that show potential triggering by nearby impact craters (Fig. 1). These landslides are properly mapped, analyzed, and dated in order to correlate them with near impact structures. All the landslides are located on the outer rim of the crater that triggered them, and, in most cases, they developed within a second, older pre-existing impact crater. The selected cases are located in the equatorial regions of Ceres and at mid-latitudes in the northern hemisphere. The uneven distribution of the analyzed landslides across the surface of the dwarf planet is related to image quality and appropriate surface illumination, both of which are necessary for detailed age determination.

Following the main classification systems[1,3], the mapped landslides have been categorized into three primary types based on the observed movement: (i) slides, (ii) flows, and (iii) complex movements. Each type exhibits distinct kinematic, morphological, and morphometric characteristics, influenced by both the geological and morphological setting of the area.

Slides are characterized by a well-defined scar deeply incised in the bedrock, followed downslope by a thick, relatively undeformed deposit with limited mobility. Flows, on the other hand, exhibit a pronounced but often irregularly shaped scar that is generally less incised than that of slides; these are followed by moderately thick, highly elongated deposits with relevant mobility and localized flow structures. Finally, complex movements display intermediate characteristics between the two previously described types, featuring well-defined and regular scars, along with relatively elongated accumulations of moderate mobility.

Morphological analysis

We have analyzed morphological and morphometric characteristics of the landslides and the craters using the high-resolution global mosaic of Ceres acquired by the Framing Camera on the NASA Dawn spacecraft during the low altitude mapping orbits (LAMO) mission phase[45]. The altimetric analyses are performed using the high-resolution global shape model of Ceres[46], by applying the stereo-photoclinometry technique developed at the Jet Propulsion Laboratory by processing Dawn's Framing Camera data. The processed images achieve a resolution of up to 35 m px-1, and the global shape model was constructed with 100-m grid spacing. The final topography was generated relative to the mean ellipsoid, which ranges from −7.3 km to 9.5 km, with an average total height error of 10.2 m[46].

To identify and map landslides on Ceres, we employ the visual interpretation criteria typically used to identify terrestrial landslides through satellite image analysis. These criteria include parameters such as shape, size, tone, mottling, texture, spatial arrangement of elements, site topography, and its environmental context[5]. The boundaries of the landslides are delineated through photointerpretation and morphological analysis. This allows surface structures such as scarps, striations, embankments, lobate forms, and deposit accumulations to be identified. These features are differentiated based on surface morphology, boundary sharpness, and slope interruptions, and this is further supported by morphological analysis derived from the HAMO global digital terrain model. The delineated boundaries for each landslide have subsequently been verified by cross-referencing with the available literature[6,20,26,29].

The morphometric characteristics of the landslides reflect their movement kinematics as well as the morphological and geological setting of the slope (Table 2). However, this study focuses only on selected landforms of particular relevance to absolute dating; therefore, the morphometric parameters do not necessarily represent the global characteristics of landslides on Ceres, for which specific studies should be consulted[6]. Despite their partial nature, the obtained results are consistent with the previously cited scientific literature on landslides[6,20,26,29].

The total landslide area (S_l) encompassing both the scar and the landslide deposit is derived using the same global shape model[46] and high-resolution global mosaic[45]. S_l ranges from 17.06 to 74.26 km², while the mobility, expressed by the H/L ratio, varies from 0.08 to 0.30. The analyzed landslides show rather high mobilities, which is in good agreement with a hypothesis of direct triggering due to meteoric impact, and may also reflect the effect of warm ice or meltwater generated by impact heating[6,26].

Dating of surface features

The quality of dating depends on the spatial resolution of the planetary images. In addition, on the analyzed surfaces, it is desirable but not mandatory to have a statistically significant number of craters[47]. In order to analyze the CSFD, impact craters are visually identified on the 35 m px-1 global mosaic[45]. The analysis focuses exclusively on craters with a diameter greater than 6 pixels (corresponding to a real diameter of about 210 m). This lower threshold is proposed as a consequence of the observation that the standard number of 10 pixels[48,49] is not sufficient for accurate analyses. Image quality (illumination and viewing geometry conditions) and landslide size are considered to determine this lower limit. This allows us to obtain a higher amount of data for the construction of the CSFD curves. The selected areas have a homogeneous appearance and are large enough to be affected by an adequate number of impact craters. In particular, the crater counting surface should be as flat as possible to avoid effects of slope degradation processes and of reduced impact flux, as these factors can lead to an inaccurate surface dating.

Following the established criteria, the analysis focuses only on the flat landslide deposits (thus excluding the scarp) and those craters characterized by homogeneous and thick ejecta layers. The portions of the deposits in the shade or with reduced visibility are excluded from the crater counting. In addition, landslides associated with craters lacking ejecta layers are also excluded from the study. Once the areas have been identified, a manual census of impact craters is made using the JMars (Java Mission-planning and Analysis for Remote Sensing) Crater Counting tool, developed by ASU's Mars Space Flight Facility, which allows the perimeter of the crater to be fitted to a circle of a given diameter (Fig. 5).

Secondary craters and fragmented single impactor craters

In the event of an impact, there is a possibility that the impactor will fragment prior to impact, or the impact event alternatively produces material through the spallation process. This may result in the formation of secondary impact craters (SICs), which have the capacity to influence the interpretation of a surface and consequently produce inconsistencies in its absolute dating[50,51]. In particular, when studying small sample areas, one of the main challenges is the presence of secondary craters, which can alter the CSFD[52,53]. In addition, using sampling areas smaller than the total surface area of the feature to be dated may lead to increased uncertainty. However, the values obtained are still adequate and representative of the age[54]. In order to obtain a reliable CSFD, only primary impact craters are generally considered[42,43]. In most cases, the distinction between primary and SICs can be determined through morphological analysis, as these craters present unique characteristics. SICs and fragmented single-impactor craters (FSICs) usually have shallow and irregular shapes and are clustered or arranged in arrays, sometimes with distinctive herringbone patterns[55–57]. SICs/FSICs may be challenging to identify should they form at a considerable distance from the primary impact site, and their removal necessitates particular caution[50,51].

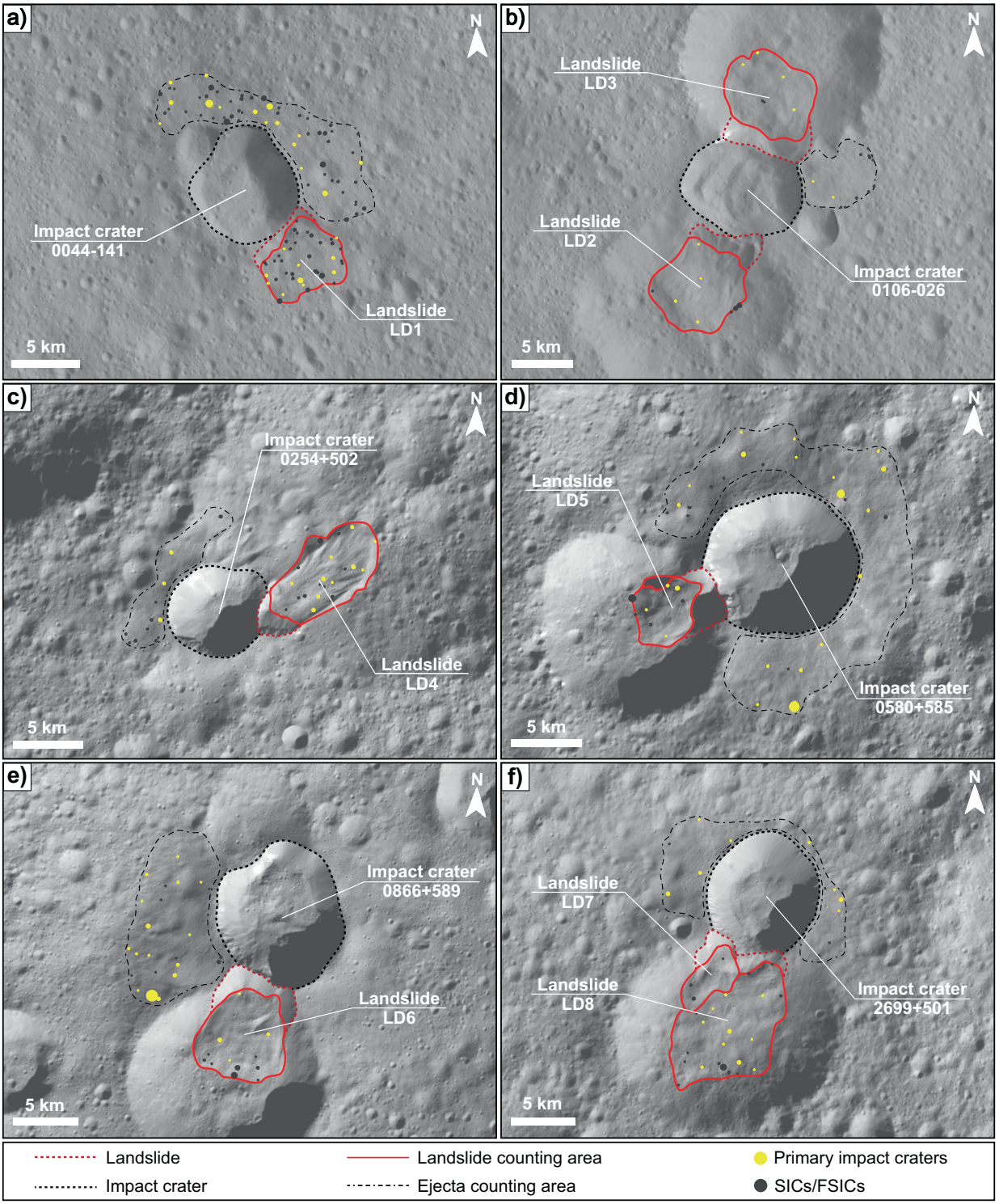

Fig. 5 | Crater counting on landslide deposits and impact crater ejecta. The maps show the analyzed areas and counted craters (divided into primary and SICs/FSICs). Panels refer to: **a** LD1; **b** LD2 and LD3; **c** LD4; **d** LD5; **e** LD6; **f** LD7 and LD8. The maps were produced with the LAMO (Low Altitude Mapping Orbits) global mosaic. Source: NASA/JPL-Caltech/UCLA/MPS/DLR/IDA.

Considering image resolution and uncertainties for discrimination of SICs/FSICs, a dual approach for absolute dating is used in this study. The first approach encompasses all craters, thereby providing statistically more robust information, while the second approach considers solely primary craters. The analysis and removal of SICs/FSICs for the construction of the CSFD have been the subject of several works, as evidenced by the extensive research in this area[41,58–60]. The present paper employs a method properly developed to remove SICs/FSICs from the analyzed populations[40]. The method is based on the manual detection and classification of features and construction of Voronoï tessellation to eliminate areas not affected by primary craters. For craters with diameters >210 m, primaries are distinguished from SICs and FSICs. In this way, only the primary impact craters and their relative area are used for the construction of CSFDs and absolute dating of the landslides.

Absolute dating of landslides and triggering craters

The absolute model age of impact craters potentially triggering landslides is determined using an approach similar to that used for landslides[40]. The absolute dating of the most relevant impact craters (i.e., those near landslide scarps) is performed only on the clearest and most distinct landforms—specifically, those where crater counting can be conducted optimally. To ensure accuracy, the dating process focuses on the most prominent and thick ejecta deposits (or portions thereof), minimizing the risk of including craters associated with the underlying unit. Nevertheless, there is a possibility that some older and larger craters remain visible through the ejecta, even in the thicker portions used for crater counting. Since these older craters do not provide reliable information on the real age of the ejecta, they are not included in the construction of CSFD and in the absolute dating of the impact structures.

The CSFDs are examined through the software CraterStats II[42,58], available from http://hrscview.fu-berlin.de/software.html. For this study, the collected data are analyzed with the production and the chronology function developed for Ceres[24], using the lunar-derived model chronology system. Model ages are derived using the Poisson timing analysis, which allows obtaining meaningful results even for small areas and few or no craters at all[47].

Reporting summary

Further information on research design is available in the Nature Portfolio Reporting Summary linked to this article.

Data availability

The dataset includes the inventory of eight landslides on the dwarf planet Ceres, mapped and measured to enable reproducible morphometric analyses. Data are available at https://doi.org/10.5281/zenodo.17623744.

Received: 11 June 2025; Accepted: 9 December 2025;
Published online: 22 December 2025

References

1. Varnes, D. J. Slope movement types and processes. in *Landslides: Analysis and Control* (eds Schuster, R. L. & Krizek, R. J.) 11–33 (National Academy of Sciences, 1978).
2. Brunetti, M. T. & Peruccacci, S. Landslides in the solar system. in *Oxford Research Encyclopedia of Planetary Science* https://doi.org/10.1093/acrefore/9780190647926.013.254 (Oxford University Press, 2023).
3. Hungr, O., Leroueil, S. & Picarelli, L. The Varnes classification of landslide types, an update. *Landslides* **11**, 167–194 (2014).
4. Bickel, V. T., Aaron, J., Manconi, A., Loew, S. & Mall, U. Impacts drive lunar rockfalls over billions of years. *Nat. Commun.* **11**, 2862 (2020).
5. Brunetti, M. T. et al. Analysis of a new geomorphological inventory of landslides in Valles Marineris, Mars. *Earth Planet. Sci. Lett.* **405**, 156–168 (2014).
6. Chilton, H. T. et al. Landslides on Ceres: inferences into ice content and layering in the upper crust. *J. Geophys. Res. Planets* **124**, 1512–1524 (2019).
7. Discenza, M. E., Esposito, C., Komatsu, G. & Miccadei, E. Large-scale and deep-seated gravitational slope deformations on Mars: a review. *Geosciences* **11**, 174 (2021).
8. Discenza, M. E. et al. Evidence for landslides in Sisyphi Cavi (Noachis Terra, Mars): Slope evolution and role of endogenous preparatory factors. *Icarus* **425**, 116314 (2025).
9. Pajola, M. et al. The pristine interior of comet 67P revealed by the combined Aswan outburst and cliff collapse. *Nat. Astron.* **1**, 0092 (2017).
10. Ruj, T. et al. Recent boulder falls within the Finsen crater on the lunar far side: an assessment of the possible triggering rationale. *Icarus* **377**, 114904 (2022).
11. Kumar, S. P. et al. Gullies and landslides on the Moon: evidence for dry-granular flows. *J. Geophys. Res. Planets* **118**, 206–223 (2013).
12. Xiao, Z., Zeng, Z., Ding, N. & Molaro, J. Mass wasting features on the Moon – how active is the lunar surface? *Earth Planet. Sci. Lett.* **376**, 1–11 (2013).
13. McColl, S. T. Landslide causes and triggers. in *Landslide Hazards, Risks, and Disasters* 13–41 https://doi.org/10.1016/B978-0-12-818464-6.00011-1 (Elsevier, 2022).
14. Melosh, H. J. *Planetary Surface Processes* (Cambridge University Press, 2011).
15. Neuffer, D. P. & Schultz, R. A. Mechanisms of slope failure in Valles Marineris, Mars. *Q. J. Eng. Geol. Hydrogeol.* **39**, 227–240 (2006).
16. Lucchitta, B. K. Landslides in Valles Marineris. *Mars. J. Geophys. Res. Solid Earth* **84**, 8097–8113 (1979).
17. Malin, M. C. Mass movements on Venus: preliminary results from Magellan cycle 1 observations. *J. Geophys. Res. Planets* **97**, 16337–16352 (1992).
18. Tesson, P.-A. et al. Evidence for thermal-stress-induced rockfalls on Mars impact crater slopes. *Icarus* **342**, 113503 (2020).
19. Bishop, J. L. et al. Martian subsurface cryosalt expansion and collapse as trigger for landslides. *Sci. Adv.* **7**, eabe4459 (2021).
20. Duarte, K. D. et al. Landslides on Ceres: diversity and geologic context. *J. Geophys. Res. Planets* **124**, 3329–3343 (2019).
21. Johnson, B. C. & Sori, M. M. Landslide morphology and mobility on Ceres controlled by topography. *J. Geophys. Res. Planets* **125**, e2020JE006640 (2020).
22. Sierks, H. et al. The dawn framing camera. *Space Sci. Rev.* **163**, 263–327 (2011).
23. Buczkowski, D. L. et al. The geomorphology of Ceres. *Science* **353**, aaf4332 (2016).
24. Hiesinger, H. et al. Cratering on Ceres: implications for its crust and evolution. *Science* **353**, aaf4759 (2016).
25. Sizemore, H. G. et al. A global inventory of ice-related morphological features on dwarf planet Ceres: implications for the evolution and current state of the cryosphere. *J. Geophys. Res. Planets* **124**, 1650–1689 (2019).
26. Schmidt, B. E. et al. Geomorphological evidence for ground ice on dwarf planet Ceres. *Nat. Geosci.* **10**, 338–343 (2017).
27. Le Becq, N., Conway, S. J., Jabaud, B., Tobie, G. & Artoni, R. A new model of crater degradation on Ceres involving ice sublimation and talus formation. *Icarus* **428**, 116353 (2025).
28. Hughson, K. H. G. et al. The Ac-5 (Fejokoo) quadrangle of Ceres: geologic map and geomorphological evidence for ground ice mediated surface processes. *Icarus* **316**, 63–83 (2018).
29. Parekh, R. et al. Influence of volatiles on mass wasting processes on Vesta and Ceres. *J. Geophys. Res. Planets* **126**, e2020JE006573 (2021).
30. Ruesch, O. et al. Cryovolcanism on Ceres. *Science* **353**, aaf4286 (2016).
31. Blance, A. J. et al. Lobate forms around craters on the moon and Mercury: origin from landslides, ejecta flows and modification stage collapse. *J. Geophys. Res. Planets* **130**, e2025JE008980 (2025).
32. Scaioni, M. et al. Recognition of landslides in lunar impact craters. *Eur. J. Remote Sens.* **51**, 47–61 (2018).
33. Guimpier, A. et al. Dynamics of recent landslides (<20 My) on Mars: insights from high-resolution topography on Earth and Mars and numerical modelling. *Planet. Space Sci.* **206**, 105303 (2021).
34. Molaro, L., Discenza, M. E., Minnillo, M., Komatsu, G. & Miccadei, E. Absolute dating and evolutionary model of large rock avalanches on Mars: examples from the Hydraotes Chaos and Tiu Valles region. *Icarus* **407**, 115778 (2024).
35. Quantin, C., Allemand, P., Mangold, N. & Delacourt, C. Ages of Valles Marineris (Mars) landslides and implications for canyon history. *Icarus* **172**, 555–572 (2004).

36. Woodley, S. Z., Fawdon, P., Balme, M. R. & Rothery, D. A. Repeated and long-lasting fault activation on Amazonian Mars as demonstrated by tectonically induced landslides. *Geophys. Res. Lett.* **51**, e2023GL107757 (2024).
37. Boyce, J. M., Mouginis-Mark, P. & Robinson, M. The Tsiolkovskiy crater landslide, the moon: an LROC view. *Icarus* **337**, 113464 (2020).
38. Shoemaker, E. M., Hackman, R. J. & Eggleton, R. E. Interplanetary correlation of geologic time. *Adv. Astronaut Sci.* **8**, 70–89 (1963).
39. Pasckert, J. H. et al. Geologic mapping of the Ac-2 coniraya quadrangle of Ceres from NASA's Dawn mission: implications for a heterogeneously composed crust. *Icarus* **316**, 28–45 (2018).
40. Discenza, M. E., Minnillo, M., Komatsu, G. & Miccadei, E. Utilization of the Voronoï tessellation for improved planetary age determination: a case study of a large rampart crater in Thaumasia Planum (Mars). *Planet. Space Sci.* **217**, 105503 (2022).
41. Lagain, A. et al. Model age derivation of large martian impact craters, using automatic crater counting methods. *Earth Space Sci.* **8**, e2020EA001598 (2021).
42. Michael, G. G. & Neukum, G. Planetary surface dating from crater size–frequency distribution measurements: partial resurfacing events and statistical age uncertainty. *Earth Planet. Sci. Lett.* **294**, 223–229 (2010).
43. Platz, T., Michael, G., Tanaka, K. L., Skinner, J. A. & Fortezzo, C. M. Crater-based dating of geological units on Mars: methods and application for the new global geological map. *Icarus* **225**, 806–827 (2013).
44. Zeilnhofer, M. F. & Barlow, N. G. The morphologic and morphometric characteristics of craters on Ceres and implications for the crust. *Icarus* **368**, 114428 (2021).
45. Roatsch, T. et al. High-resolution Ceres low altitude mapping orbit atlas derived from Dawn framing camera images. *Planet. Space Sci.* **140**, 74–79 (2017).
46. Park, R. S. et al. High-resolution shape model of Ceres from stereophotoclinometry using Dawn Imaging Data. *Icarus* **319**, 812–827 (2019).
47. Michael, G. G., Kneissl, T. & Neesemann, A. Planetary surface dating from crater size-frequency distribution measurements: Poisson timing analysis. *Icarus* **277**, 279–285 (2016).
48. Robbins, S. J. et al. The variability of crater identification among expert and community crater analysts. *Icarus* **234**, 109–131 (2014).
49. Wang, Y., Xie, M., Xiao, Z. & Cui, J. The minimum confidence limit for diameters in crater counts. *Icarus* **341**, 113645 (2020).
50. McEwen, A. S. & Bierhaus, E. B. The importance of secondary cratering to age constraints on planetary surfaces. *Annu. Rev. Earth Planet. Sci.* **34**, 535–567 (2006).
51. Robbins, S. J. & Hynek, B. M. Distant secondary craters from Lyot crater, Mars, and implications for surface ages of planetary bodies. *Geophys. Res. Lett*. **38**, 5 (2011).
52. Neesemann, A. et al. The various ages of Occator crater, Ceres: results of a comprehensive synthesis approach. *Icarus* **320**, 60–82 (2019).
53. Xiao, Z. & Strom, R. G. Problems determining relative and absolute ages using the small crater population. *Icarus* **220**, 254–267 (2012).
54. Michael, G. & Liu, J. Planetary surface dating from crater size–frequency distribution measurements: Interpretation of small-area and low number counts. *Icarus* **431**, 116489 (2025).
55. McEwen, A. S. et al. The rayed crater Zunil and interpretations of small impact craters on Mars. *Icarus* **176**, 351–381 (2005).
56. Oberbeck, V. R. & Morrison, R. H. On the formation of the lunar herringbone pattern. *Lunar Planet. Sci. Conf. Proc.* **4**, 107 (1973).
57. Shoemaker, E. M. & Hackman, R. J. Stratigraphic basis for a lunar time scale. in *The Moon* (eds Kopal, Z. & Mikhailov, Z. K.) vol. 14 289–300 (Academic Press, 1962).
58. Michael, G. G., Platz, T., Kneissl, T. & Schmedemann, N. Planetary surface dating from crater size–frequency distribution measurements: Spatial randomness and clustering. *Icarus* **218**, 169–177 (2012).
59. Riedel, C. et al. Studying the global spatial randomness of impact craters on Mercury, Venus, and the Moon with geodesic neighborhood relationships. *J. Geophys. Res. Planets* **126**, e2020JE006693 (2021).
60. Salih, A. L., Lompart, A., Grumpe, A., Wöhler, C. & Hiesinger, H. Automatic detection of secondary craters and mapping of planetary surface age based on lunar orbital images. *Int. Arch. Photogramm. Remote Sens. Spat. Inf. Sci*. **XLII-3-W1**, 125–132 (2017).

Acknowledgements

We would like to thank Giulia Magnarini and two anonymous reviewers for their timely and helpful comments. We are grateful to Gregory G. Michael and Nico Schmedemann for fruitful discussions on surface dating.

Author contributions

M.E.D. and M.T.B. led conception, analysis, paper writing and reviewing. L.M., G.K., and E.M. contributed to paper writing and reviewing. M.M. contributed to analysis.

Competing interests

The authors declare no competing interests.

Additional information

Supplementary information The online version contains supplementary material available at https://doi.org/10.1038/s43247-025-03119-x.

Correspondence and requests for materials should be addressed to Maria Teresa Brunetti.

Peer review information *Communications Earth and Environment* thanks Hideaki Miyamoto, Giulia Magnarini and the other, anonymous, reviewer(s) for their contribution to the peer review of this work. Primary Handling Editors: Teng Wang and Alireza Bahadori. A peer review file is available.